SUPPLEMENT TO THE *WELDING JOURNAL*, SEPTEMBER 2011
Sponsored by the American Welding Society and the Welding Research Council

Comparison between DC(+) and Square Wave AC SAW Current Outputs to Weld AISI 304 for Low-Temperature Applications

A change in the electrical welding output and flux type can enhance the mechanical properties of AISI 304 stainless steels for low-temperature applications

BY R. E. TOMA, S. D. BRANDI, A. C. SOUZA, AND Z. MORAIS

ABSTRACT

Welded equipment for cryogenic applications is utilized in chemical, petrochemical, and metallurgical industries. One material suitable for cryogenic application is austenitic stainless steel, which usually doesn't present ductile/brittle transition temperature, except in the weld metal, where the presence of ferrite and micro inclusions can promote a brittle failure, either by ferrite cleavage or dimple nucleation and growth, respectively. A 25-mm- (1-in.-) thick AISI 304 stainless steel base metal was welded with the SAW process using a 308L solid wire and two kinds of fluxes and constant voltage power sources with two types of electrical outputs: direct current electrode positive and balanced square wave alternating current. The welded joints were analyzed by chemical composition, microstructure characterization, room temperature mechanical properties, and CVN impact test at –100°C (–73°F). Results showed that an increase of chromium and nickel content was observed in all weld beads compared to base metal. The chromium and nickel equivalents ratio for the weld beads were always higher for welding with square wave AC for the two types of fluxes than for direct current. The modification in the Cr_{eq}/Ni_{eq} ratio changes the delta ferrite morphology and, consequently, modifies the weld bead toughness at lower temperatures. The oxygen content can also affect the toughness in the weld bead. The highest absorbed energy in a CVN impact test was obtained for the welding condition with square wave AC electrical output and neutral flux, followed by DC(+) electrical output and neutral flux, and square wave AC electrical output and alloyed flux.

Introduction

Cryogenics can be defined as the science and technology of temperatures below –153°C (120 K). This limiting temperature was proposed based upon the boiling point of the main atmosphere gases, as well as methane, which are below this temperature (Ref. 1). According to Lebrun (Ref. 2), cryogenics arose two centuries ago from the search to liquefy the atmospheric gases considered until that time incondensable. In 1877, L. Cailletet and R. Pictet liquefied air for the first time, and in 1883, K. Olszewski and S. Wroblewski separated oxygen from nitrogen. However, the increase in cryogenics applications started in 1908, when H. Kamrelingh Onnes made the first helium liquefaction. There is also equipment in the chemical and petrochemical industries that work in temperatures as low as –100°C, which is not exactly a cryogenic application according to the definition presented above.

In both cases (cryogenics or low-temperature applications), the 300 stainless steels series is widely used, and the AISI 304 and 304L stainless steels are usually employed. They are recommended for these applications because their ductile/brittle transition temperature is negligible at temperatures above –269°C (Ref. 3). On the other hand, the ductile/brittle transition temperature in ferritic and martensitic stainless steels occurs a few degrees below zero, depending on the steel chemical composition and grain size.

According to Hertzberg (Ref. 4), the temperature effect on the necessary energy to crack the material is related in the ferritic steels to a change in the mechanism of microscopic fracture, which happens due to cleavage at low temperatures and has a brittle behavior. On cleavage, fracture occurs on the crystallographic planes of different grains, and the fracture surface presents a morphology similar to a river.

For structural applications, it is necessary to have an adequate combination between the fracture resistance (K_{Ic}, J_{Ic}, or CTOD) and the yield point (σ_y), depending on the service temperature. However, these properties are inversely proportional at any given temperature. The toughness in stainless steels, as a function of temperature, decreases monotonically with the yield point and the temperature (Refs. 5, 6).

At low temperatures above the range of cryogenic applications, stainless steels tend to fail exclusively by a ductile rupture mechanism, in which occurs a coalescence of dimples, generated by second-phase particles present in the material. Therefore, the fracture resistance is controlled by the volumetric fraction, size, distribution, and morphology of second-phase particles. The interface between second phase and the matrix can be easily separated at low plastic deformation associated with low temperatures. In this case, the

*R. E. TOMA is a graduate student, and S. D. BRANDI (*sebrandi@usp.br*) is associate professor, University of São Paulo, Metallurgical and Materials Engineering Department, São Paulo, Brazil. A. C. SOUZA and Z. MORAIS, Lincoln Electric do Brasil, Guarulhos, São Paulo, Brazil.*

KEYWORDS

Cryogenics
Low Temperature
Stainless Steel
Petrochemical
Submerged Arc Welding

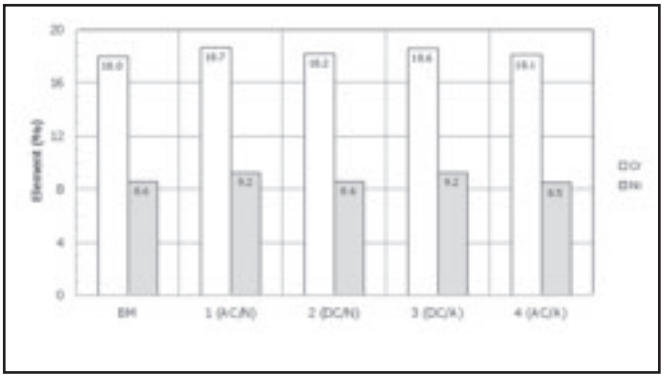

Fig 1 — Chromium and nickel contents in weld beads according to the experimental conditions used in this work.

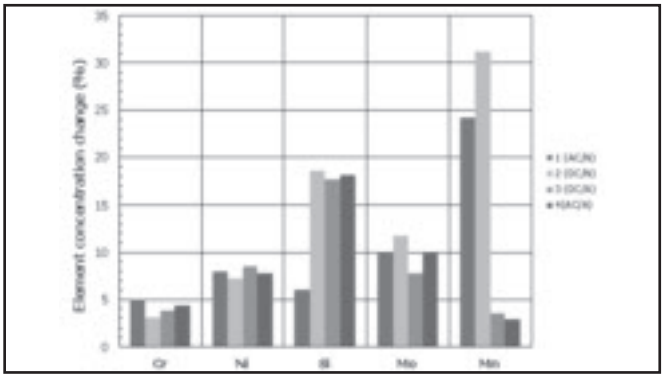

Fig. 2 — Change in weld metal chemical composition as a function of experimental welding conditions. Weld metal is compared to base metal chemical composition.

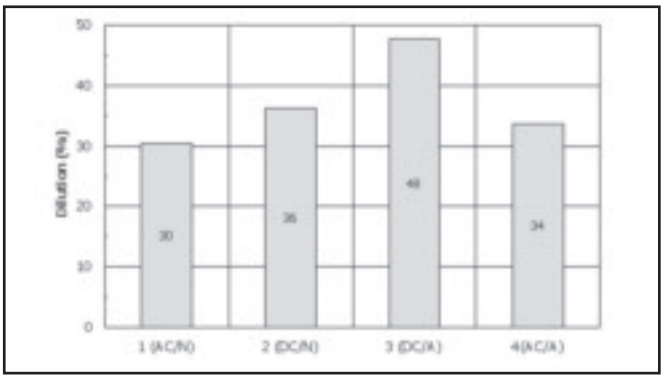

Fig. 3 — Dilution in weld bead as a function of experimental welding conditions.

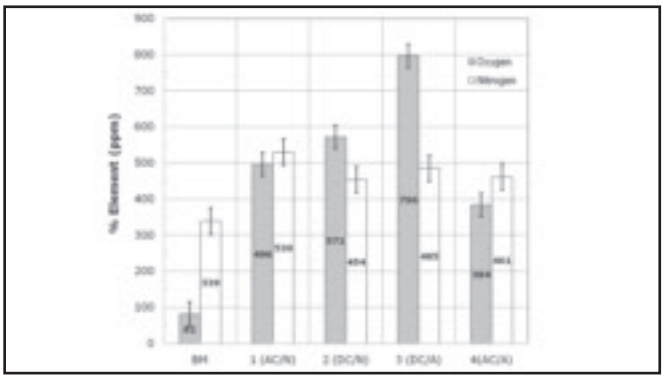

Fig. 4 — Comparison among oxygen and nitrogen contents for base metal (BM) and four experimental weld metal conditions.

toughness measured by Charpy V-notch (CVN) absorbed impact energy or crack tip opening displacement (CTOD) decreases with temperature.

Furthermore, in the case of stainless steel weld metal, the matrix is a dual-phase type, with ferrite and austenite, depending upon the solidification mode (Refs. 7–10). The presence of ferrite, even in small amounts, usually less than 10%, can also generate a ductile or a brittle path, depending upon the test temperature. At high and room temperatures, ferrite is ductile and, consequently, its volumetric fraction and its morphology don't control the rupture mechanism. In this case, the fracture mechanism is due to the volumetric fraction of inclusions. At low or cryogenic temperatures, ferrite can be brittle and can lead to reduction in the toughness of the weld by a cleavage mechanism.

The ferrite morphology and its volumetric fraction in the weld metal are important in determining the cracking mechanism at low and cryogenic temperatures. Solidification mode, ferrite morphology, and its amount are determined

Table 1 — Tension Test Results for All Tested Samples

Experimental Condition	Number of Test	Tensile Strength (MPa) Measured	Tensile Strength (MPa) Mean	Minimum Tensile Strength (MPa)	Sample Failure Localization
1(Ac/N)	1	601	606.0	515	Weld Metal
	2	611			
2(DC/N)	1	606	607.0		
	2	608			
3(DC/A)	1	601	598.5		
	2	596			
4(AC/A)	1	604	606.0		
	2	608			

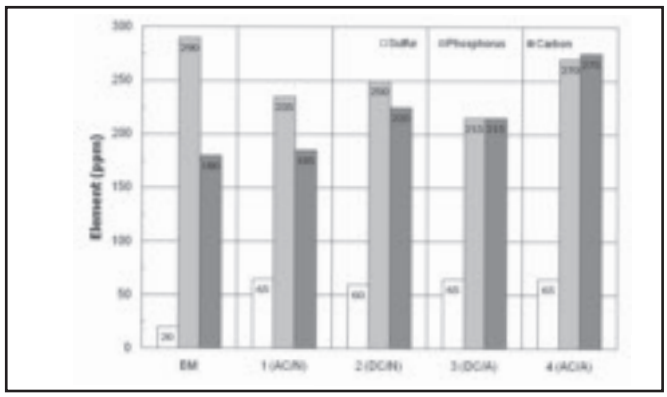

Fig. 5 — Comparison among sulfur, phosphorus and carbon contents for base metal (BM) and four experimental weld metal conditions.

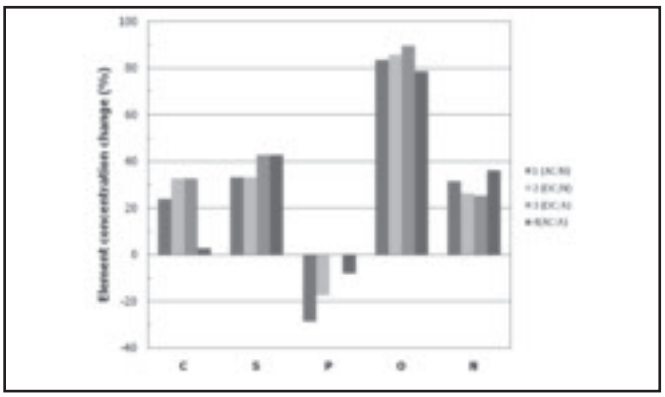

Fig. 6 — Change in C, S, P, O, and N chemical composition as a function of experimental welding conditions. Weld metal is compared to base metal chemical composition.

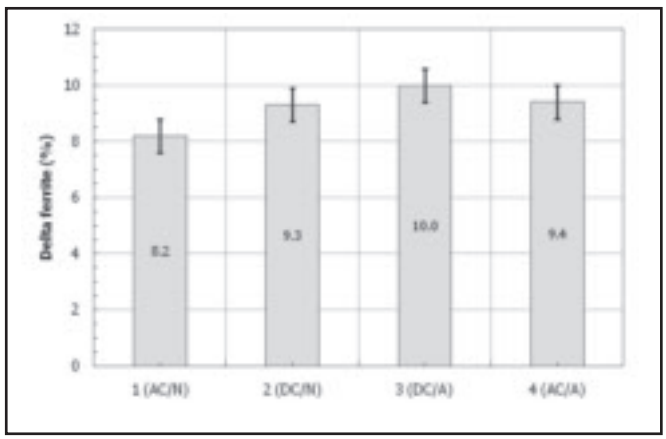

Fig. 7 — Weld bead delta ferrite content for the experimental welding conditions.

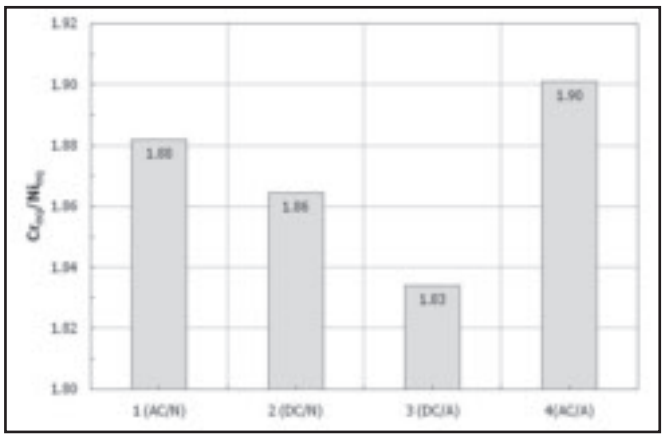

Fig. 8 — Cr_{eq}/Ni_{eq} ratio for the experimental conditions used in this work.

by chemical composition (Cr_{eq}/Ni_{eq} ratio) and by the orientation between <100>γ direction and heat flow flux direction during weld pool solidification (Refs. 11–13).

As presented before, the Cr_{eq}/Ni_{eq} ratio is one factor that determines the weld pool solidification mode, ferrite morphology, and the volumetric fraction of delta ferrite in the weld bead (Refs. 7–10). If Cr_{eq}/Ni_{eq} ratio is below 1.48, the solidification mode produces a weld bead with an austenitic microstructure. When the Cr_{eq}/Ni_{eq} ratio is between 1.48 and 1.95, a ferrite-austenite solidification mode takes place in the weld pool, which produces an austenitic-ferritic microstructure with 2 to 10% ferrite. Vermicular ferrite morphology is more frequent than lath ferrite when Cr_{eq}/Ni_{eq} ratio is in the lower part of the 1.48 to 1.95 range. Lath ferrite usually occurs more often than vermicular morphology while Cr_{eq}/Ni_{eq} ratio is closer to 1.95. As Cr_{eq}/Ni_{eq} ratio is higher than 1.95, a primary ferrite microstructure is produced in the weld bead, with austenite precipitation during cooling by ferrite decomposition.

The weld pool chemical composition can be changed due to thermochemical and electrochemical reactions on the molten droplet at the wire tip, during droplet transfer, and in the weld pool in contact with the electric arc or molten slag in submerged arc welding (SAW) and electroslag welding (ESW) processes (Refs. 14–17). According to Blander and Olson (Ref. 14), the anodic reaction (electrode positive) at the molten droplet-slag interface in the wire tip is responsible for the oxide formation, and the anodic reaction (electrode negative) of the metal ion is responsible for the electrodeposition of metals at the weld pool. The chemical composition due to cathodic reactions is adjusted by chemical reactions. Also, the welding pool chemical composition can be changed due to dilution. Usually, direct current (electrode positive) polarity produces a higher penetration and direct current (electrode negative) increases deposition rate, using the same SAW process flux type. Thus, using direct current (electrode positive) or alternating current during SAW can produce a different chemical composition in the weld pool. Therefore, the change in chemical composition can alter the ferrite morphology. The heat flow flux condition can also affect the ferrite morphology. In the case where <100>γ directions and heat flow

Table 2 — Charpy V-Notch Test Results at –100°C (–73°F) for All Experimental Conditions

Experimental Condition	Mean Absorbed Energy (J)	Mean Lateral Expansion (mm)
1(AC/N)	65 ± 5	0.783 ± 0.097
2(DC/N)	56 ± 5	0.740 ± 0.068
3(DC/A)	36 ± 5	0.661 ± 0.087
4(AC/A)	53 ± 6	0.694 ± 0.134

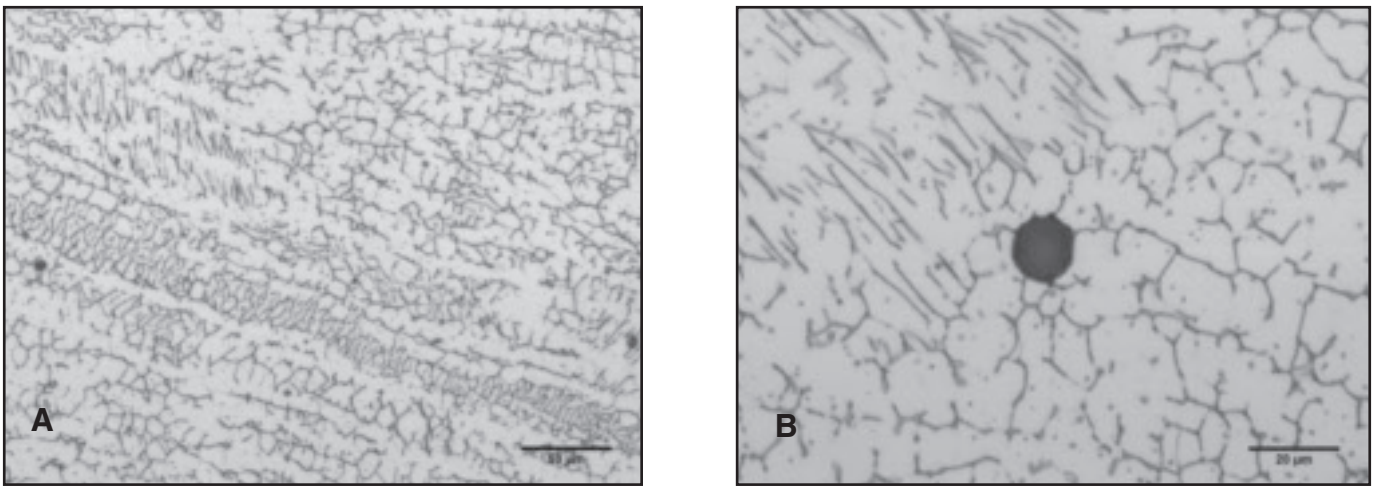

Fig. 9 — Typical ferrite morphology for 3(DC/A) weld metal experiment. A — Presents both ferrites morphologies types; B — detail of a ferrite transition morphology region. Electrolytic etching: oxalic acid 10%. Optical microscope.

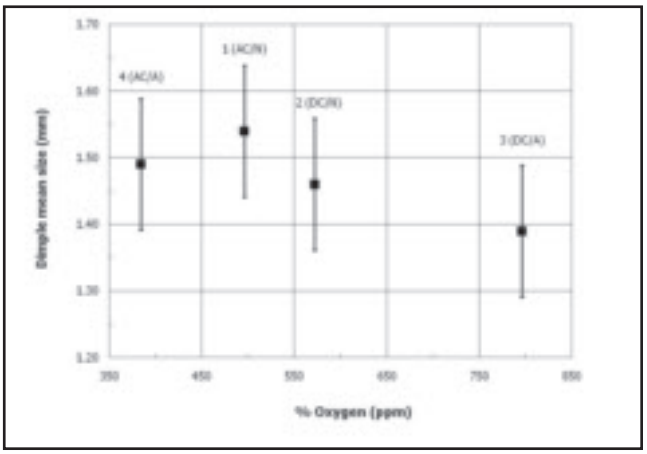

Fig. 10 — Dimple mean size as a function of oxygen content in weld metal for the experimental conditions tested in this work.

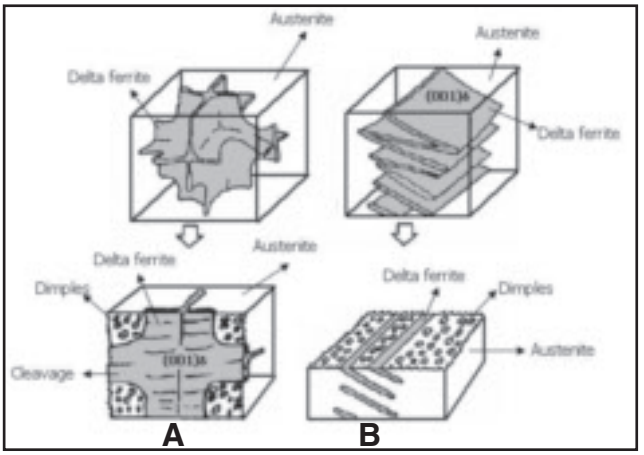

Fig. 11 — Mechanism of low and cryogenic temperatures for two ferrites morphologies Refs. 11,12. A — Vermicular ferrite morphology B — lath ferrite morphology.

flux direction during weld pool solidification are parallel, delta ferrite can be formed with a lath or vermicular morphology, depending upon the existence, or not, of Kurdjumov-Sachs orientation relationship between delta ferrite and austenite (Ref. 12). On the other hand, if the <100>γ direction and heat flow direction during weld pool solidification are not parallel, the delta ferrite morphology is vermicular (Ref. 12).

These delta ferrite morphologies and volumetric fraction are also related to the toughness of the microstructure. Depending upon the temperature, a small-scale yielding (cryogenic temperature) or a large-scale yielding (low temperature, room temperature, and above) condition takes place during crack propagation. Lath ferrite usually presents better toughness than vermicular ferrite in an austenitic-ferritic matrix for small-scale yielding (Ref. 12). This is due to the crack propagation in the ferrite at low or cryogenic temperatures. Vermicular ferrite is usually a more continuous and aligned ferrite than lath ferrite, which has a ferrite crack propagation mean path lower than vermicular ferrite, mainly due to the ductile austenite that acts as a crack arrester.

The objective of this work is to determine the differences in chemical composition and low-temperature mechanical properties of an AISI 304 base metal weld joint caused by changing submerged arc welding parameters such as flux type (neutral and alloyed fluxes) and electric condition (direct current electrode positive or square wave alternating current).

Experimental Procedure

A 25-mm- (1-in.-) thick AISI 304 stainless steel base metal was welded by the SAW process using an AWS A5.9 ER308L filler metal with 3.25-mm (⅛-in.) diameter and two kinds of fluxes: neutral and chromium autocompensating alloyed. The welds were made by a constant voltage power source with two electrical output types: direct current electrode positive and balanced square wave alternating current. Samples 1 and 4 were made with alternating current, balanced square wave with a 70-Hz frequency with neutral (AC/N) and chromium autocompensating alloyed fluxes (AC/A), respectively. Samples 2 and 3 were welded with continuous current electrode positive, using neutral (DC/N) and chromium autocompensating alloyed fluxes (DC/A), in that order. All four samples were welded with a mean heat input close to 2.2 kJ/mm (0.87 kJ/in.) and a double-V bevel type.

The welded joints were analyzed by different methods. The chemical composition of base metal, weld metal, and filler metal were analyzed using an optical emission spectroscopy and LECO® equipment for carbon, sulfur, oxygen, and nitrogen measurements. Dilution was determined by a ratio between melted base metal area to weld metal area. Microstructure characterization was done using an optical microscope and scanning electron microscope with an energy dispersive microanalysis. Samples observed in the optical microscope

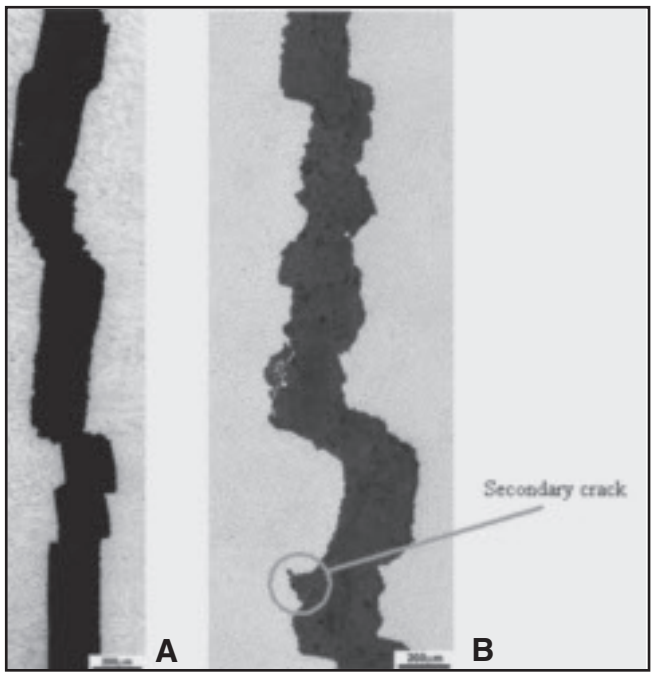

Fig. 12 — A view of CVN crack propagation. A — Flat propagation type in sample 3DC/A; B — rounded propagation type for sample 4(AC/A).

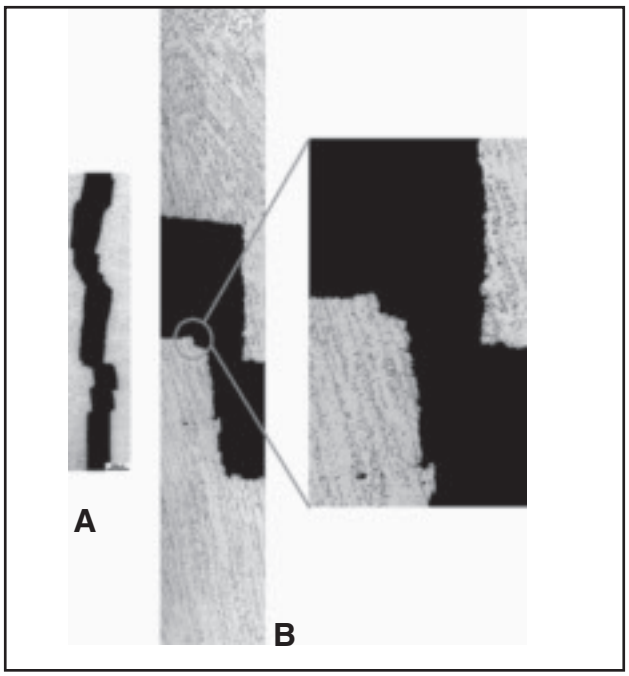

Fig. 13 — A view of CVN crack propagation for sample 3(DC/A). A — Low magnification picture of crack path; B — a close-up of a sample region.

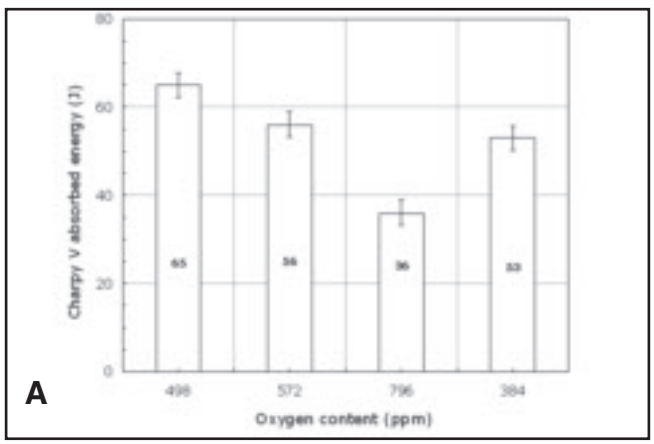

Fig. 14 — A correlation between CVN results at and weld metal oxygen content. A — CVN absorbed energy ; B — lateral expansion.

were electrolyticaly etched using a 10% solution of oxalic acid. The volumetric fraction of ferrite in the weld metal was measured by a magnetic technique, using a ferritoscope equipment.

Mechanical properties were measured at room temperature (tensile test) and CVN notch-toughness impact test at –100°C (–73°F), repeated five times sample per welding condition. Charpy sample surface fractures were also observed in a scanning electron microscope.

Results and Discussion

Chemical Composition

The Cr and Ni chemical composition of the weld beads is presented in Fig. 1 for all experiments. Analyzing these values, one can notice an increase in chromium content for all welding conditions. The highest values were achieved welding with a neutral flux and a balanced square wave alternating current electrical output (AC/N) followed by welding with an alloyed flux (chromium compensating flux) and a balanced square wave alternating current electrical output (AC/A). The result for AC/A condition was expected, since an alloyed flux was utilized to compensate for variations in chromium content during welding. On the other hand, the increase in chromium content using a neutral flux and a balanced square wave alternating current (AC/N) should be explained by other ways besides flux type, such as electrical output and weld bead dilution.

As an AC square wave electrical output was used, the change in chemical composition can be related to the change in polarity during welding by electrochemical reactions. When the welding pool is negative during AC welding, a Cr electrochemical reaction takes place, depositing chromium, nickel, and other metals. When the polarity is changed to positive, a Cr oxidation in the welding pool occurs. The opposite reactions occur in the molten droplet at the wire tip. To analyze these reactions, a change in element content of the weld metal was compared to the base metal chemical composition. A positive-value means a pickup of the element in the weld pool. The result is depicted in Fig. 2.

In analyzing Fig. 2, all tested welding conditions presented Cr and Ni contents higher than in the base metal. The chromium content using the AC/Neutral flux condition presented almost the same amount of AC/A flux, and both presented a higher increase in chromium content in the weld pool than DC/N and DC/A

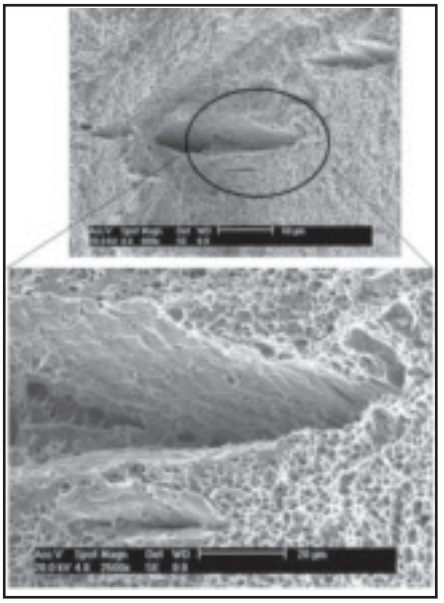

Fig. 15 — A fracture surface of sample 1(AC/N), presenting a dimple ductile type in austenite and cleavage fracture of ferrite, in a different plane.

fluxes. These results follow the same trend proposed by Frost et al. (Ref. 15) when they analyzed the increase in chromium content, by electrochemical reaction, comparing AC and DC submerged arc welding of a carbon steel. In these results, they used an AC wave with a sinusoidal shape. When an AC square wave is utilized for welding, the arc voltage and welding current are almost kept in the setup value, with almost no change when compared to a sinusoidal wave shape. Thus, the electrochemical reactions using a square wave shape are maintained with same charge density for each half cycle, given a favorable electrochemical reaction rate compared to sinusoidal wave shape.

Dilution can also affect the chemical composition of weld metal, since it represents the base metal portion in the weld metal, which usually has a higher amount of impurities than base metal. Thus, the higher the dilution, the lower the amount of impurities, taking into account only the base metal melted volume and the deposited filler metal volume. Figure 3 shows the dilution of weld metal for AC and DC experimental conditions. Analyzing this figure, the AC electrical output depicted a dilution lower than DC electrical output, for same flux type. Submerged arc welding process typically presents a high penetration in DC(+) and a high deposition rate in DC(–) electrical output. As the AC electrical output is a balanced square wave, these two effects act a half time each during the AC current cycle, justifying the difference between DC(+) and AC dilution results. Examining the same electrical output and different flux types, the neutral flux presents a lower dilution than the alloyed flux, which also correlated to oxygen quantity in the weld pool.

Usually, for DC(+), the increase in the amount of oxygen increases the penetration of the weld bead, which can also raise the dilution of the weld bead. In the case of AC welding, the change in polarity can alter the amount of oxygen due to electrochemical reactions. Figure 4 presents the amount of oxygen and nitrogen in weld metal for the experiments.

The oxygen weld metal amount in DC electrical output follows the same trend presented by the weld joint dilution. The change in dilution with oxygen content may be caused by a Marangoni flow induced by the amount of oxygen in the weld bead. In the case of AC electrical output, the electrochemical reaction produces the same trend in weld metal oxygen content, which is lower than in DC electrical output. These behaviors are similar to the results reported by Frost (Ref. 15) for carbon steels. The amount of oxygen in weld metal is also a function of the basicity index (BI) of the flux. The neutral flux used in this work has a BI of 2.70, and the alloyed flux presents a BI of 0.97. The higher the BI, the lower is the content of oxygen in the weld bead, reaching up to a minimum constant amount of oxygen, for DC (+) and carbon steels (Refs. 18, 19). The results for stainless steels follow the same trend, when comparing results for the same electrical output. Nitrogen weld metal content does not present a significant change with the experimental conditions.

The amount of C, S, and P are also important for weld bead shape and cryogenic or low-temperature mechanical properties. The amount of these elements in weld metal may be also controlled by an electrochemical reaction. In the case of carbon and phosphorus, the neutral flux presented a higher pickup of these elements than the alloyed flux for the DC(+) condition. The dilution of DC/A should be taken into account to analyze these compositions since DC/A presented the highest dilution and, consequently, less impurities were introduced into the weld pool. Comparing this result for AC electrical output, the result is opposite mainly due to the different chemical composition of the welding flux; that is, the increase in carbon and phosphorus is higher for the alloyed flux. Also, the dilution of the AC output weld bead has almost the same dilution, and the effect of the melted base metal has almost the same influence in the chemical composition of these weld beads. Figure 5 depicts the carbon, sulfur, and phosphorus for the experimental conditions.

To analyze the effect the electrical output has on weld metal chemical composition, a change of C, S, P, O, and N elements is compared to base metal chemical composition. These results are shown in Fig. 6.

There is no change in carbon pick up for DC(+) and the two flux types. On the other hand, in the AC condition, there is an increment in the carbon content for neutral flux when compared to alloyed flux. Examining the carbon pickup, AC electrical output presented a lower value than DC(+), for both flux types. These results show a trend similar to the carbon pickup by electrochemical reaction reported in Ref. 16.

Investigating the sulfur composition change in the weld bead, it was found change occurs only when the electrical output is changed, and it is kept constant for the same flux type. In this case, the sulfur pickup in weld metal may be due to the change in the flux basicity, which is related to the desulfurization reaction in the weld pool that is enhanced by a basic slag produced by a basic flux.

In the case of a change of phosphorus in the weld bead, there was a loss of this element for all experiments. For the same electrical output, the reduction in P was higher for same flux type and neutral, which is a basic flux type, than for alloyed flux. In this case, a dephosphorization reaction takes place, which is promoted by flux with a high basicity index. Also, the electrochemical reaction acts together to reduce the P amount, as suggested by Ref. 16.

The change in oxygen content also follows the effect of the flux basicity index and electrochemical reactions, as discussed previously.

Metallographic Characterization

Delta Ferrite Volumetric Fraction

Delta ferrite volumetric fraction was measured by magnetic measurements, using a Ferritoscope, in seven different regions along a weld bead cross section. The results of ferrite mean value are presented in Fig. 7. All experimental conditions presented a ferrite volumetric fraction below 10%, as usually recommended for welding with 300 austenitic stainless steel series. All delta ferrite volumetric fractions have closer values. The higher amount of delta ferrite was found in condition 3(DC/A) followed by condition 4 (AC/A), condition 2 (DC/N), and condition 1(AC/N). These results should be analyzed by the pickup of all alloying elements that are present in the chromium and nickel equivalent equations in particular for the alloying elements with higher amounts, such as Cr and Ni.

As presented previously, the delta ferrite morphology can be predicted by the chromium equivalent/nickel equivalent ratio. Figure 8 presents Cr_{eq}/Ni_{eq} ratio for the experiments. According to the results shown in Fig. 8, samples with a Cr_{eq}/Ni_{eq}

ratio close to 1.95 tends to produce more lath ferrite than vermicular ferrite morphology. On the other hand, a Cr_{eq}/Ni_{eq} ratio close to 1.8 tends to produce more vermicular ferrite than lath ferrite morphology. The AC electrical output produced a weld bead microstructure with more lath delta ferrite than vermicular ferrite. In the case of a DC(+) welding condition, the Cr_{eq}/Ni_{eq} ratio is lower for alloyed flux than for neutral flux. The condition 3(DC/A) presented the lower Cr_{eq}/Ni_{eq} ratio, which means a tendency to produce more vermicular ferrite than lath ferrite. Figure 9 depicts a typical microstructure of AISI 304 stainless steel weld bead for 3(DC/A) experiment.

Figure 9A presents a typical microstructure for both ferrite morphologies, lath and vermicular, predominating vermicular ferrite. Figure 9B shows a detail of a microstructure transition region, with lath ferrite morphology in the left upper corner and vermicular ferrite in the lower right corner. Figure 9B depicts also an oxide microinclusion in the transition region.

Ferrite morphology is also influenced by the heat flow flux direction compared to <100>γ direction (Refs. 12, 13). In the case where both are parallel in austenite, the ferrite formed may be vermicular or lath type, depending upon the existence of Kurdjumov-Sachs (KS) orientation relationship between austenite and delta ferrite. In the case where there is a KS orientation relationship and also the heat flow is also parallel to <100>δ ferrite direction, the lath ferrite morphology is produced. On the other hand, vermicular ferrite morphology is produced if there is no KS relationship between ferrite and austenite, even though the heat flow and <100>δ directions might be parallel. If the heat flow flux direction and <100>δ directions are not parallel, vermicular or lath ferrite are produced. In the case where the heat flow flux direction is not parallel to <100>γ direction, independent of a KS relationship between ferrite and austenite, a vermicular morphology is produced. During weld pool travel, there is a change in the heat flow to <100> direction. As a consequence, a change in ferrite morphology by this mechanism takes place, justifying why vermicular and lath ferrite morphology are always present in a microstructure of a ferrite/austenite solidification mode.

Mechanical Properties

Tension Test

Results for tension tests are depicted in Table 1. Observing these results, condition 3(DC/A) presented the lowest tensile strength. The mechanism of a ductile fracture in a tensile test sample is related to dimple (microvoid) nucleation at inclusions, growth, and coalescence. Therefore, the elevated content of oxygen in the weld metal, as condition 3(DC/A) presented, is an indication of a large quantity of microinclusions present in the microstructure, and consequently, the tensile strength resulted in a lower resistance value.

The relationship between tensile strength and oxygen weld metal content are confirmed in Fig. 10. In this figure, the dimple mean size was measured in SEM surface fracture for all tension test samples. As the dimple mean size decreases, the rate of microvoid nucleation at the inclusions in the weld metal increases, which means a higher volumetric fraction of inclusions and, consequently, high oxygen content in the weld bead, as condition 3(DC/A). After nucleation, dimples grow and coalesce up to the final sample rupture. The other three conditions presented almost the same dimple mean size, which is compatible to the mechanical property measured.

CVN Test

Table 2 shows the result of Charpy V-notch test at –100°C (–73°F). Analyzing these results, one notices experiment 3(DC/A) depicted the lowest absorbed energy and lateral expansion of all experiments. In the tested temperature, the fracture of the four samples was mainly by dimple coalescence in austenite and cleavage in ferrite. In other words, at this temperature there is large-scale yielding, where the sample rupture exhibits some ductility, which can be correlated to measured lateral expansion. Experiment 3(DC/A) presented the lowest mean lateral expansion of the four tested conditions. This result can also be explained by the same mechanism presented previously in the tension test. The oxygen content is one factor that affects this result, in particular to the austenitic part of the weld bead microstructure, which has a large amount of oxide inclusions. As these tests were done at low temperature, ferrite cleavage can occur during crack propagation. Ferrite can crack by a twinning mechanism acting in the slip system {112}<111> or in the {100} planes. The family direction in ferrite twinning is the same of KS orientation relationship in ferrite. This coincidence in direction can alter the toughness of ferrite morphology at low temperature, suggesting a lower toughness to lath ferrite morphology. This is not the case, since the ferrite cleavage crack mean free path should be taking into account. So, vermicular ferrite has a larger mean free path than lath ferrite and, consequently, vermicular ferrite is less tough than lath ferrite. This is in accordance to Refs. 12 and 13, where it is reported that lath ferrite has a higher toughness than vermicular ferrite for cryogenic temperatures, depending on crack direction propagation and also ferrite cleavage. Figure 11 presents the mechanism proposed by Refs. 12 and 13.

According to the Inoue-proposed mechanism (Refs. 12, 13), there are dimple nucleation and growth at inclusions in austenite and cleavage of ferrite in {100} planes in the case of vermicular ferrite morphology. For lath ferrite morphology, there is only dimple nucleation and growth with no ferrite cleavage. As a consequence, this failure behavior is responsible for a tougher microstructure, composed mainly by lath ferrite morphology in an austenitic matrix.

The CVN test crack propagation path was observed in optical microscope for the tested conditions, in a plane parallel to the crack plane and in the half thickness of CVN test samples. Two different crack paths types were observed, one with a tendency to a rounded shape and the other with a more flat appearance, respectively, for 1(AC/N), 2(DC/N), 4(AC/A) experiments, and 3(DC/A) experiment. Comparing these path types and the absorbed energy, experiment 3(DC/A) presented the lowest CVN absorbed energy and lateral expansion. Figure 12 shows this two path types for two experiments, 3(DC/A) and 4(AC/A).

Analyzing 3(DC/A) experiment microstructure, depicted in Fig. 13, one can notice the vermicular-type microstructure in this sample, as was predicted by the Cr_{eq}/Ni_{eq} ratio. This microstructure presents an oriented pattern, which facilitates the crack propagation. Observing the center of austenite dendrite, there are a lot of oxide inclusions promoting the crack by a dimple nucleation and growth mechanism at CVN test temperature, for the two crack propagation types shown in Fig. 12. Observing the fracture surface in the detail of Fig. 14B, the profile suggests this mechanism together with ferrite cleavage mechanism, as presented in Fig. 11A. Thus, a relationship between CVN absorbed energy, CVN lateral expansion and the oxygen content in the weld bead is expected, as Fig. 14 depicts.

The lower CVN absorbed energy and lateral expansion of sample 3(DC/A) is also explained by amount of oxygen content, as presented previously.

Examining the surface fracture of samples 1(AC/N), 2(DC/N), and 4(AC/A), another phenomenon was observed, which is the presence of secondary cracks, in a plane with a different angle to main crack propagation plane. Figure 12B shows one example. The observation of surface fracture in SEM depicted a ductile-type crack with regions presenting a delta ferrite cleavage, as observed in Fig. 15. All samples presented a CVN absorbed energy higher than sample 3(DC/A), and since austenite is ductile at the temperature test, the microstructure has more lath ferrite, and the amount of oxygen was lower for

these samples. The presence of secondary cracks by ferrite cleavage is an enhancing toughness mechanism, which can produce CVN absorbed energy higher than an energy obtained only by a pure mechanism of dimple nucleation and growth, as presented schematically in Fig. 11B. The presence of secondary cracks can also explain the higher toughness of lath ferrite when compared to vermicular ferrite, as observed experimentally in References 11 and 12.

Conclusions

Based on the materials, welding procedure, and results analysis techniques one can conclude the following:

1) There is a difference in the weld bead chemical composition when the balanced AC square wave electrical output is used for welding AISI 304 stainless steel, for both fluxes. The amounts of chromium and nickel were increased when compared to the base metal chemical composition for all experiments. The best results were obtained for the samples welded with active flux using square wave AC current type followed by neutral flux and square wave AC current. Same trend was observed for oxygen and phosphorus. In the case of oxygen, there was a pickup of oxygen, which presented the lowest values for square wave AC current, both flux types, and the highest value to DC(+) and alloyed flux. In the case of P, a dephosphorization reaction took place in the weld pool and the amount of this element was decreased for all experiments. The P lost was higher for AC balanced square wave and neutral flux. Some results among experimental conditions may be influenced by the weld bead dilution that was higher for DC/A flux experimental condition.

2) The Cr_{eq}/Ni_{eq} ratio was greater for balanced square wave AC than for DC(+), for both flux types. AC/A flux condition presented the highest ratio (1.90), followed by AC/neutral flux (1.88) and DC/neutral flux (1.86). The lowest value was obtained by DC/A flux condition (1.83). These results can be arranged in two groups: one with a higher Cr_{eq}/Ni_{eq} ratio (1.86–1.90 range) and another with a lower Cr_{eq}/Ni_{eq} ratio (1.83). The former presents a microstructure with more lath ferrite than vermicular ferrite morphology. The second group presented a microstructure composed mainly of vermicular ferrite, with some amount of lath ferrite.

3) Although all samples achieved a resistance higher than the minimum required by the standard, tension test results presented a lower tensile strength for sample DC/alloyed flux. The mechanism of fracture is controlled by dimple nucleation, growth, and coalescence. Dimple is nucleated at oxide inclusions, which volumetric fraction can be inferred by oxygen content. The higher the oxide volumetric fraction, the nucleation rate is higher and the dimple size is decreased when coalescence takes place. DC/alloyed flux presented the highest amount of oxygen of all tested conditions, and as a consequence, the lowest dimple mean size measured at the tension test surface fracture.

4) The CVN impact test at –100°C (–73°F) showed the best result for samples welded with square wave AC and neutral flux followed by DC(+) polarity and neutral flux; square wave AC and alloyed flux; and DC(+) polarity and alloyed flux, respectively. These results were analyzed taking into account the oxygen content and ferrite morphology, which is related to the ferrite cleavage and ferrite orientation in the microstructure. The mechanism of failure in stainless steel weld metal CVN samples can be by a ductile mechanism (dimple nucleation and growth in austenite) or by a brittle mechanism (delta ferrite cleavage and crack mean free path). The CVN sample with lowest absorbed energy presented the highest amount of oxygen and also a vermicular ferrite morphology, which is a more continuous and aligned type.

5) Secondary cracks were observed in all samples with a predominant lath ferrite. The ferrite cleavage occurs in a plane with different orientation to the main crack propagation plane. This is a mechanism to enhance the toughness of the lath ferrite microstructure.

Acknowledgment

The authors appreciate the welding of the samples and also the funding for mechanical tests and chemical analysis provided by Lincoln Electric of Brazil.

References

1. Lebrun, P. 2007. An introduction to cryogenics. European Organization for Nuclear Research, CERN/AT 2007-1.

2. Lebrun, P. 2003. Cryogenics, Key to Advanced Science and Technology. *Bulletin of the IIR*, N° 2003-6.

3. Michler, T. 2007.Toughness and hydrogen compatibility of austenitic stainless steel welds at cryogenic temperatures. *International Journal of Hydrogen Energy*, Vol. 32, pp. 4081–4088, .

4. Hertzberg, R. W. 1996 *Deformation and Fracture Mechanics of Engineering Materials*. John Wiley & Sons Inc., 4th ed, pp. 375–378.

5. Tobler, R. L., Siewert, T. A., and McHenry, H. I. 1986. Strength-toughness relationship for austenitic stainless steel welds at 4 K. Fracture and Deformation Division, National Bureau of Standards, USA.

6. Chi, K., McLean, M. S., McPherson, and M. A., Baker, T. N. 2007 Single sided single pass submerged arc welding of austenitic stainless steel. *Materials Science and Technology* 23(9): 1039–1048.

7. Lippold, J. C., and Savage, W. F. 1980. Solidification of austenitic stainless steel weldments: Part II — The effect of alloy composition on ferrite morphology. *Welding Journal* 59(2): 48s to 58s.

8. Suutala, N., Takalo, T., and Moisio, T. 1979. The relationship between solidification and microstructure in austenitic and austenitic-ferritic stainless steel welds. *Met. Trans*. 10A(4): 512–514.

9. Takalo, T., Suutala, N., and Moisio, T. 1979. Austenitic solidification mode in austenitic stainless mode in austenitic stainless steel welds. *Met. Trans*. 10A(8): 1173–1181.

10. Suutala, N., Takalo, T., and Moisio, T. 1983. Ferritic-austenitic solidification mode in austenitic stainless steel welds. *Met. Trans*. 14A(2): 191–197.

11. Elmer, J. W., Allen, S. M., and Eagar, T. W. 1989. Microstructural development during solidification of stainless steel alloys. *Met. Trans*. 20A(10): 2118–2131.

12. Inoue, H., Koseki, T., Fuji, M., and Nishimoto, K. 2001. Formation mechanism of different ferrite morphologies and effect of ferrite morphology on cryogenic impact toughness and pitting corrosion resistance in austenitic stainless steel weld metals. *Quarterly Journal of the Japan Welding Society*, 19(1): 100–113.

13. Kamiya, O., Kumagai, K., and Futami, T. 1994. Effect of ferrite morphology on fracture mode of stainless steel weld metal. *Welding International* 8(10): 798–803.

14. Blander, M., and Olson, D. L. 1986. Electrochemical effects on weld pool chemistry in submerged arc and DC electroslag welding. *Proceedings International Conference on Trends in Welding Research*, ed. S. David, ASM, May 18–22, Gatlinburg, Tenn., pp. 271–277.

15. Frost, R. H., Olson, D. L., and Edwards, G. R. 1983. The influence of electrochemical reactions on the chemistry of eletroslag welding process. *Modeling of Casting and Welding Process II Eng. Conf. Proceedings*, eds. J. A. Dantzig and J. T. Berry, Met. Soc. AIME, pp. 279–294.

16. Indacochea, J. E., Blander, M., Christensen, N., and Olson, D. L. 1985. Chemical reactions during submerged arc welding with FeO-MnO-SiO_2 fluxes. *Met. Trans.*, 16B(6): 237–245.

17. Tuliani, S. S., Boniszewski, and T., Eaton. N. F. 1969. Notch toughness of commercial submerged arc weld metal. *Weld. Met. Fabr*. 37(8): 327–339.

18. Ekström, U., and Olsson, K. 1980. The influence of ferrite and oxygen contents on weld metal mechanical properties of submerged-arc welded stainless steels. *Weld Pool Chemistry and Metallurgy, Int. Conf.*, London, UK, April 15–17, pp. 323–334.